SUPPORTING INFORMATION:

Physical Science of the Didodecyldimethylammonium Bromide – Water System: 1. Equilibrium Phase Behaviour

Louisa Reissig,*[ab‡] Wim Pyckhout-Hintzen,[c] Simon Dalgleish,[a] Andrew R. Mount,[a] Michael E. Cates,[b‡] David Fairhurst*[b] and Stefan E. Egelhaaf [d]

[a] School of Chemistry, The University of Edinburgh, Edinburgh EH9 3JJ, United Kingdom.
[b] SUPA, School of Physics and Astronomy, The University of Edinburgh, Edinburgh EH9 3JZ, United Kingdom.
[c] Jülich Centre for Neutron Science (JCNS-1), Forschungszentrum Jülich, 52428 Jülich, Germany.
[d] Condensed Matter Physics Laboratory, Heinrich-Heine-University, 40225 Düsseldorf, Germany.
‡ Now: LR: Freie University Berlin, Germany; MEC: University of Cambridge, UK.
* To whom correspondence should be addressed: Louisa_Reissig@gmx.de, david.fairhurst@ed.ac.uk

Experimental

1. Details of the analytical methods (TLC, ESI-MS and NMR) used.
2. Additional information about the Raman setup (Fig. S1) and the correction/reduction of the strong fluorescent background (Fig. S2).
3. Additional information about the Raman microscopy setup: temperature control (Fig. S3), occurring artefacts (Fig. S4).
4. Comparison between the two Raman setups used (Fig. S5).
5. Additional details about the performed single molecule calculations.

Results

1. ESI-MS (Fig. S6) and NMR (Fig. S7) analysis of the recrystallized DDAB sample, confirming high purity.
2. Degradation pathway of DDAB at high temperature (Fig. S8).
3. Additional characterisation of the low-temperature phase transition associated with the melting of hydrated DDAB crystals (Fig. S9).
4. Additional Raman spectra of the aqueous DDAB solution (Fig. S10) and analysis of the water peak (Table S1).
5. Characterisation of the crystal structure of the DDAB zero-hydrate $\boldsymbol{X}$ and low-temperature hydrate $\boldsymbol{XW_n}$ (Fig. S11).

References

[Laughlin 1990] R.G. Laughlin et al., J. Phys. Chem., 1990, 94, 2546.
[CCCBDB 2006] CCCBDB. http://ccbdb.nist.gov/, 2006.
[Laughlin 1994] R.G. Laughlin, Academic Press, London, 1994.
[Laughlin 2009] R.G. Laughlin, *private communication*, 2009.

Experimental

Analytical methods

Thin-layer chromatography (TLC)

TLC was used to assess the impurities in DDAB samples, caused by thermal degradation. A chloroform:methanol:water:formic acid mixture (100:20:1:4) was used as the developing solvent as it is ideally suited to distinguish between quaternary ammonium salts and its amine, a likely decomposition product [Laughlin 1990]. After elution the spots were visualised using a PMA stain (Polymolybdic acid:ethanol, 10g:100ml).

Electrospray ionization mass spectroscopy (ESI-MS)

ESI-MS was used to detect impurities in DDAB due to analogues of different chain lengths. An LCQ classic mass spectrometer was used [parameter: scan mode = +c ESI Full MS (150.00 – 2000.00), source temperature = 67.97°C, capillary temperature = 180.20°C, ion injection time = 141.38 ms, elapsed scan time = 1.98 s]. Samples were dissolved in methanol and spectra recorded in the 1+ mode, so that the ion mass for each peak could be directly displayed and analysed using the Xcalibur software.

Nuclear Magnetic Resonance Spectroscopy (NMR)

^{1}H-NMR and ^{13}C-NMR were used to confirm the molecular structure of DDAB and its degradation products, and to estimate the water content in the solid samples. The basic ^{1}H-NMR and ^{13}C-NMR measurements were performed on an ARX250MHz spectrometer (default parameters ^{1}H-NMR: 16 scan, acquisition time = 4.358s, delay time = 1.000 s; ^{13}C-NMR: decoupled, 256 scans, acquisition time = 1.114 s, delay time = 1.000 s). The more advanced spectra (decoupled ^{1}H-NMR, DEPT135 and HSQC) were measured on an ARX600MHz spectrometer. The samples were dissolved in deuterated solvents: acetonitrile (CD_3CN), methanol (CD_3OD) or chloroform ($CDCl_3$). The measured spectra were analysed with the MestReNova software.

Raman Spectroscopy:

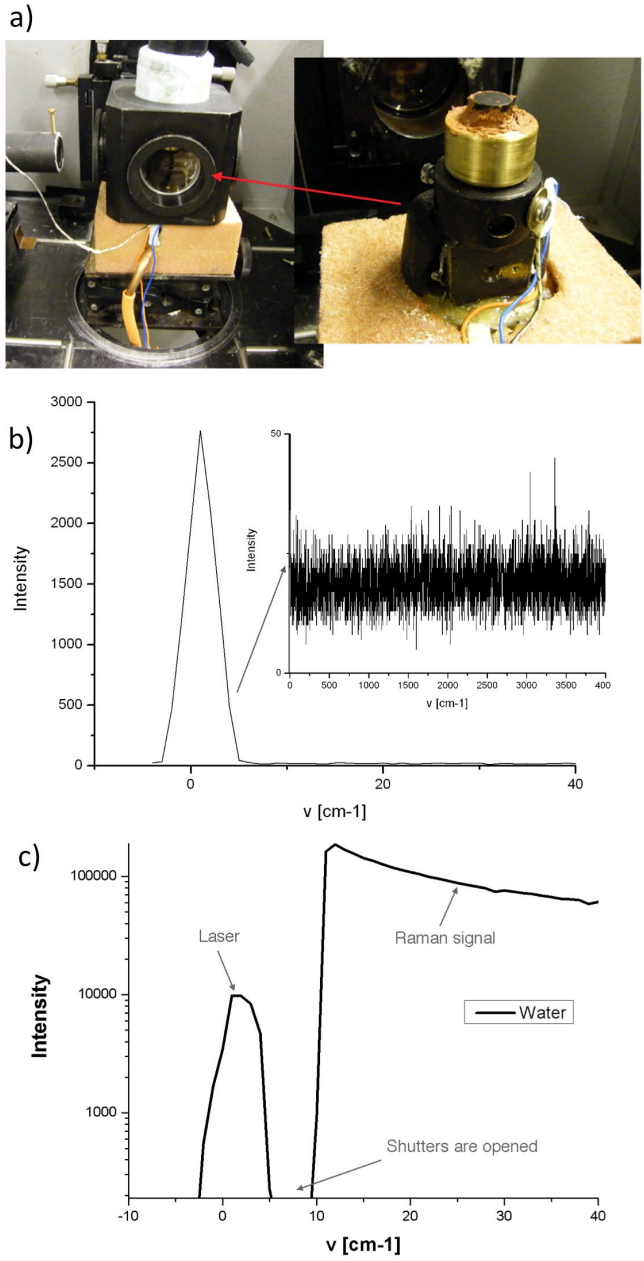

FIGURE S1: (a) Sketch of the home-build temperature control used for Raman experiments: the metallic cage is cooled with liquid nitrogen. A heating element is placed into a cylinder containing liquid nitrogen, controlling the speed of evaporation through a tube which leads to the temperature controlling stage. The sample vial is adhered to that stage with fine copper grain to ensure high thermal contact. The chamber is filled with cold dry air to prevent condensation. (b) Confirmation of the absence of emission lines (other than the line used as an excitation source), which might appear in the spectrum, by radially reducing the laser power. (c) Low-wavenumber limit of the Raman spectrum due to the opening of the shutter system. The closed shutters reduced the intensity by 107 during the scan of the first wavenumbers. The band at $\nu = 0$ cm^{-1}, corresponding to the scattered laser light is used for wavenumber correction. The Raman signal of the sample can be obtained from $\nu \geq 25$ cm^{-1}.

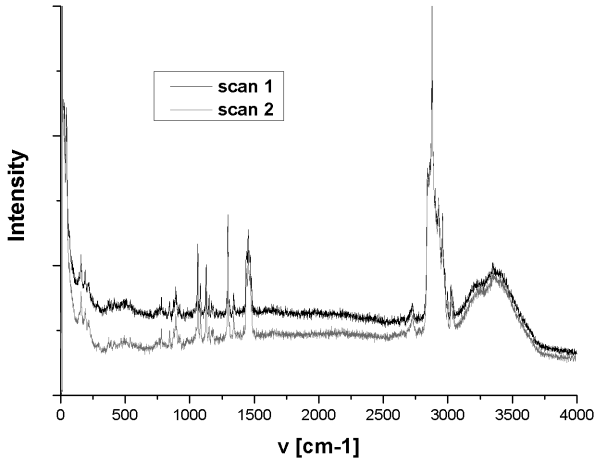

FIGURE S2: Fluorescence background in the Raman spectrum of opaque samples (scan 1), and its decrease after treating the sample with a pulse of intense laser power prior to measurement (scan 2). The observed background was approximated by a polynomial fit and removed from the spectrum using Wire 2.0. This correction was difficult for the region below 300 cm^{-1} due to the existence of a broad and intense band, the height and slope of which was consequently affected.

Raman microscopy

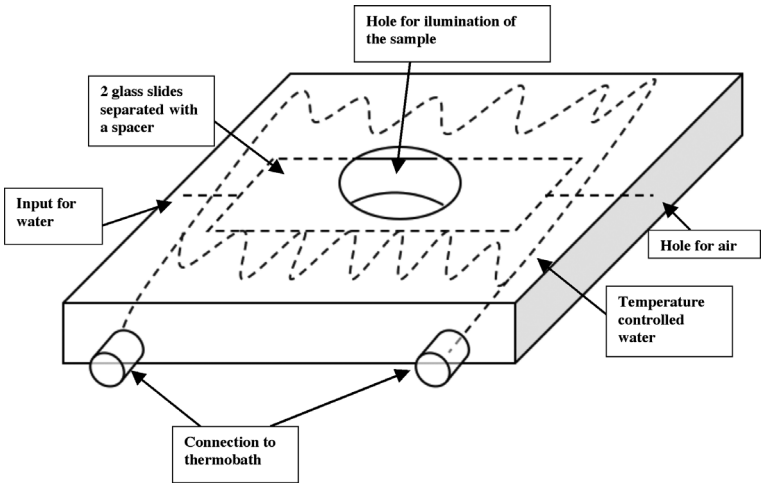

FIGURE S3: Sketch of the temperature-controlled sample cell used for Raman microscopy. The cell was made of an aluminum alloy, which ensures good thermal conductivity, whilst being easy to manipulate in shape. The temperature control was ensured by the incorporation of an extended channel for a cooling liquid (here water) into the cell, connected to a thermo-regulated bath with a cooling function. The cell was designed to surround a sample, placed on two microscope slides, separated by a spacer of thickness b = 100 µm. The sample cell was calibrated using a thermocouple placed between the glass slides, leading to a temperature accuracy of 0.5°C, stable over a long period of time and no gradient within the sample cell could be detected.

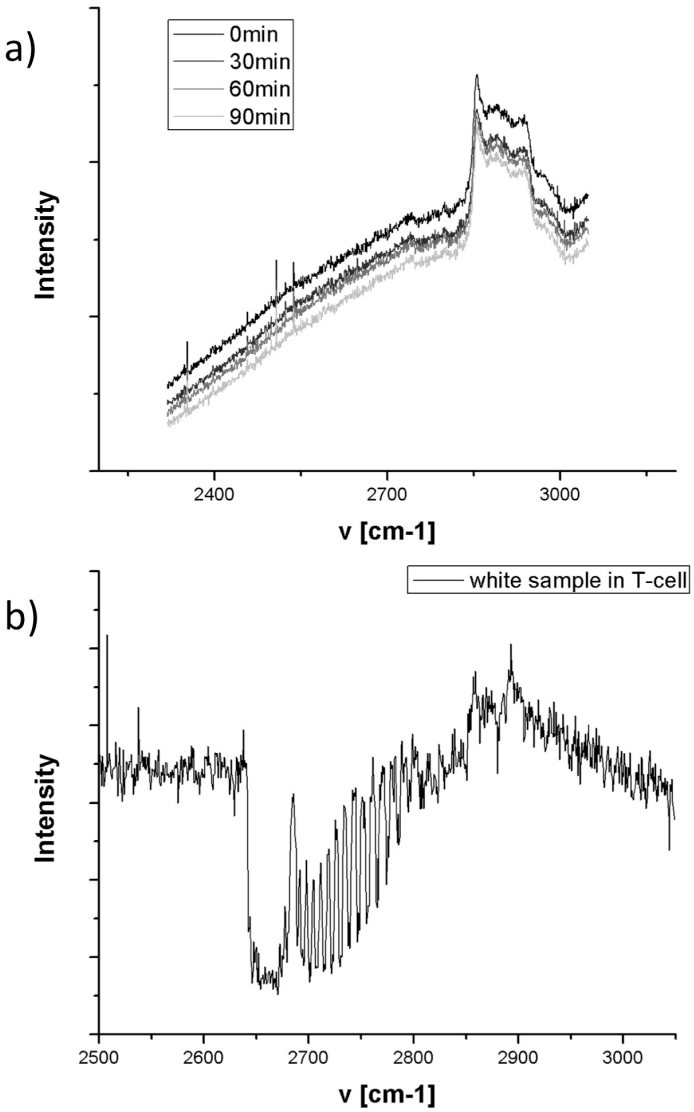

FIGURE S4: Remaining artifacts in Raman microscopy, after removing sharp peaks in the spectrum which occurred due to the failure of some pixels in the CCD camera (by recording 2 regions of the spectrum slightly shifted with respect to each other and comparing the peaks, these artefacts were identified and removed using LabSpec4.18): (a) decrease in fluorescence background with time, which could affected the shape of the water peak above 3000 cm^{-1} and (b) artifacts, caused by the strong reflection of the laser on the 'white' samples and the metallic sample cell, which could be removed by covering the sample-cell with a matt black plate with a hole of about 1 cm diameter.

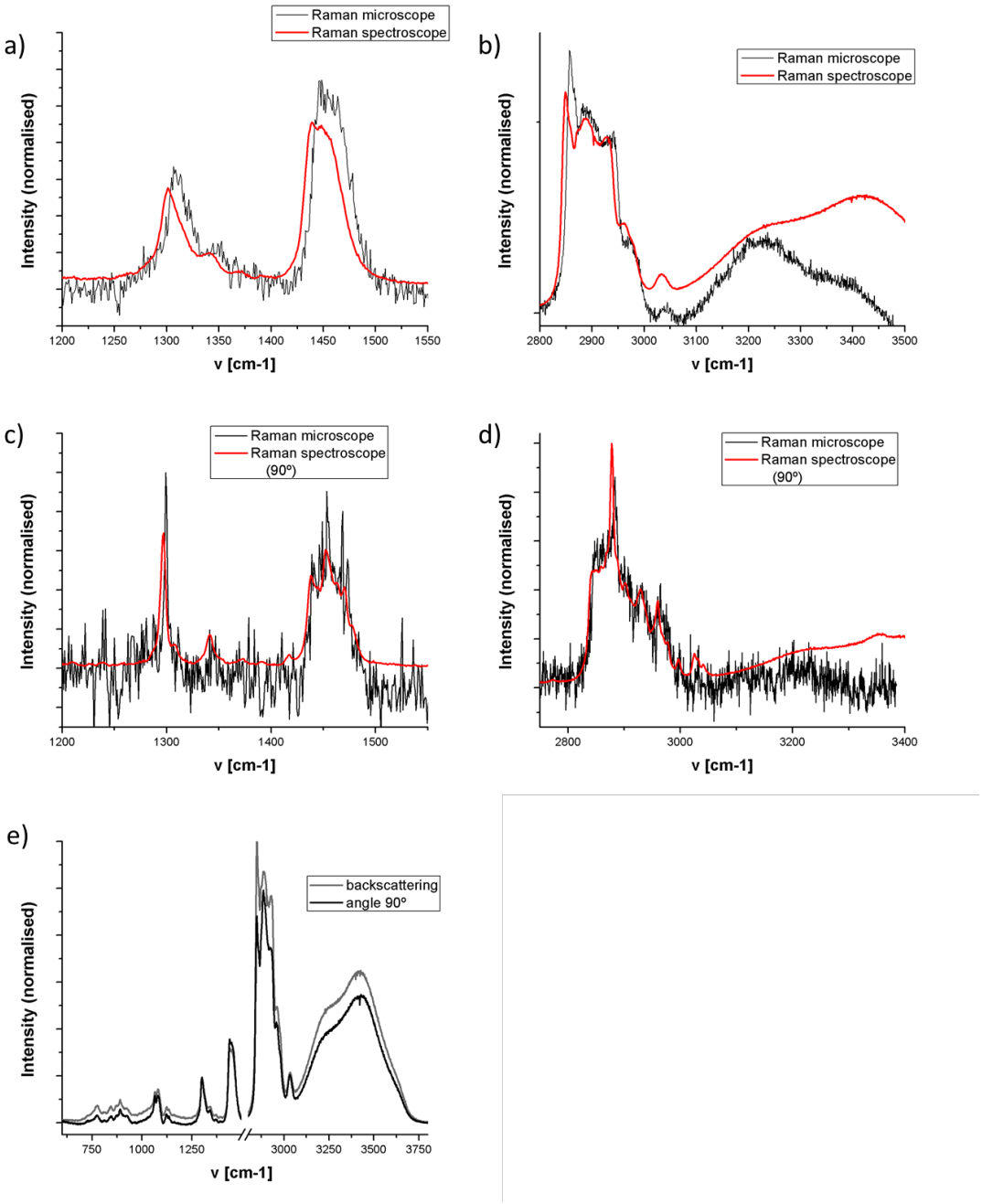

FIGURE S5: (a-d) Comparison of the spectra obtained by Raman spectroscopy (red) and microscopy (black), for the lamellar phase (a,b), and the 'white' phase (c,d). Shifts in wavenumber can be explained by the comparably poor calibration of the Raman microscopy setup, while changes in relative peak intensity especially in the region of 2800-3100 cm^{-1} were caused by the different detection geometry used in the setups: Raman signal was recorded at an angle of 90° and 180° in the spectrometer or Raman microscope, respectively. (e) comparison of the effect on the detection geometry on the spectrum obtained by Raman spectroscopy.

Single molecule calculations:

The molecules were built in ChemSketch, and the Gaussian input files were created by Arguslab. The obtained geometries and vibrational modes were investigated in GabEdit, which offered the possibility of visualizing for each frequency band the corresponding motions in the molecule, and of displaying a Raman spectrum by fitting Gaussian or Lorentzian curves of a chosen constant halfwidth to the obtained frequencies and intensities: a halfwidth of 2 was found to best reproduce the experimentally obtained shapes. The geometry optimization was carried out for various starting geometries, with varying number of gauche conformations in the alkyl chains. The required level of approximation was first tested on the all-trans geometry, which was found to be, as expected, the lowest energy configuration. For this, the geometry was optimized in 4 steps: HF 3-21G, HF 6-31G(d,p) Raman, BLYP 6-31G(d,p) Raman, B3LYP 6-31G(d,p) Raman, using the output geometry of the previous step as input geometry. While the potential energy decreased with increasing level of theory, no difference in the calculated Raman frequencies could be found when the scaling factors of the used methods were considered (0.903, 0.992, 0.961, respectively [CCCBDB 2006]). These scaling factors are based on the comparison of observed vibrational frequencies and theoretical frequencies (for each basis set), and obtained from the sum over all vibrational frequencies. The scaling factors are in general small for basis sets including polarization functinos compared to the ones without which suggests that polarisation functions are important for a good predition of vibrational frequencies. Given the sufficient approximation provided by BLYP 6-31G(d,p), as well as its lower computational cost compared to B3LYP 6-31G(d,p), BLYP 6-31G(d,p) was used for all further starting geometries to obtain the Raman spectra.

Results:

DDAB purity confirmed by ESI-MS and NMR

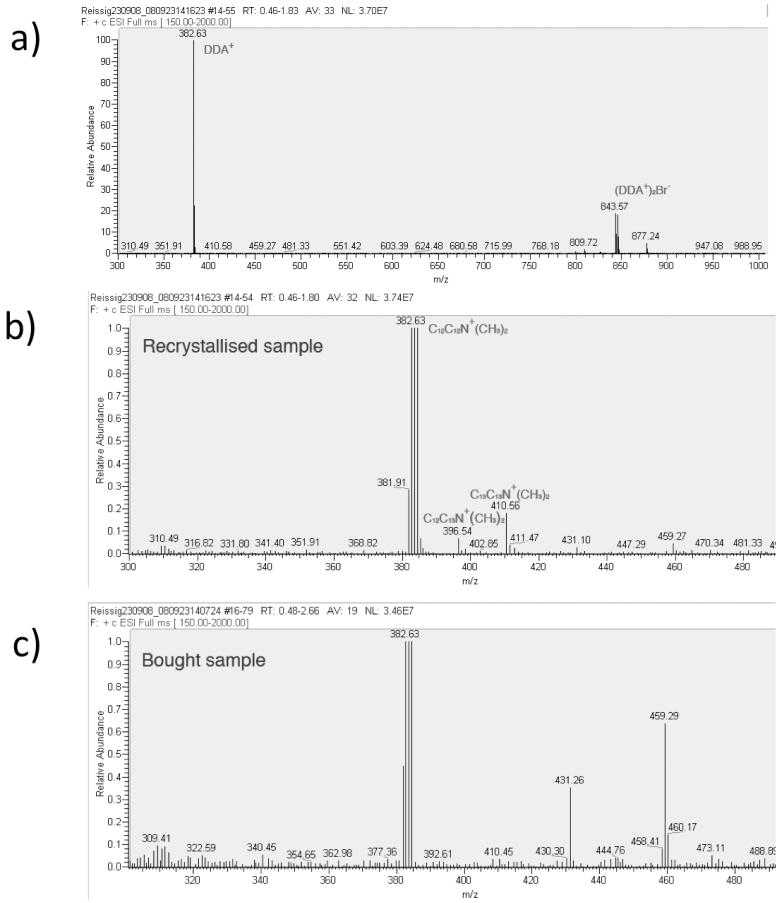

FIGURE S6: ESI MS spectra of DDAB before (a,b) and after (c) recrystallization. The main peak was assigned to DDAB: $(DDA)^+$ (expected mass in Daltons: 382.44 (100%), 383.44 (28.5%), 384.45 (4.0%)) and $(DDA)^+)_2Br^-$ (expected mass in Daltons: 843.80 (100%), 844.80 (57.0%), 844.81 (1.3%), 845.8 (97.7%), 845.81 (16.2%), 846.80 (55.5%), 846.81 (4.3%), 847.81 (16.2%), 848.81 (2.9%)). The spectrum around the main peak shows only traces (well below 1%) of the DDAB analogue $C_{12}C_{13}$DAB and $C_{13}C_{13}$DAB in the sample after recrystallization.

a)

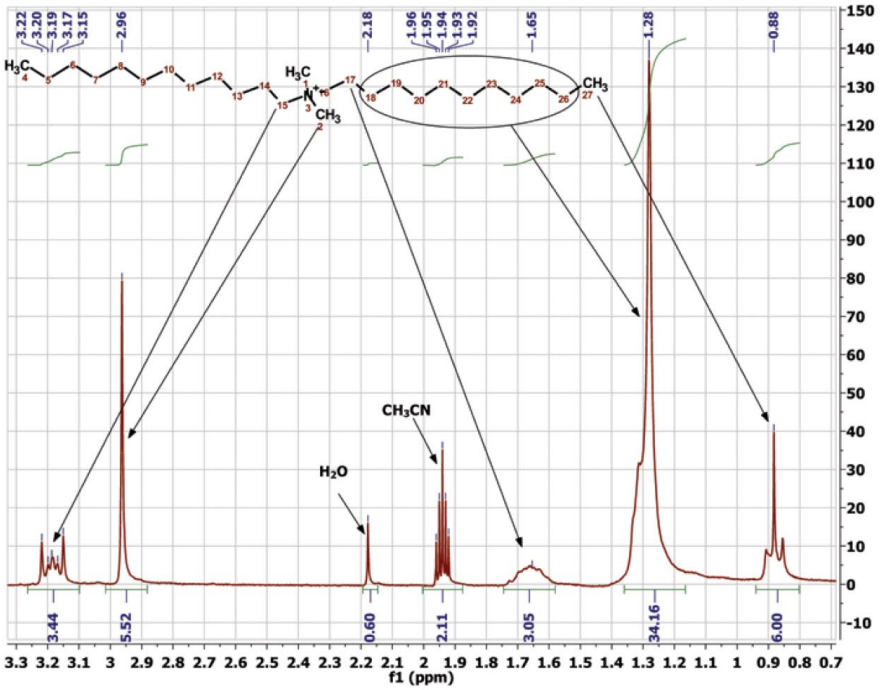
3.22
3.20
3.19
3.17
3.15
2.96
2.18
1.96
1.95
1.94
1.93
1.92
1.65
1.28
0.88
H3C
CH3
CH3CN
H2O
3.44
5.52
0.60
2.11
3.05
34.16
6.00
f1 (ppm)

b)

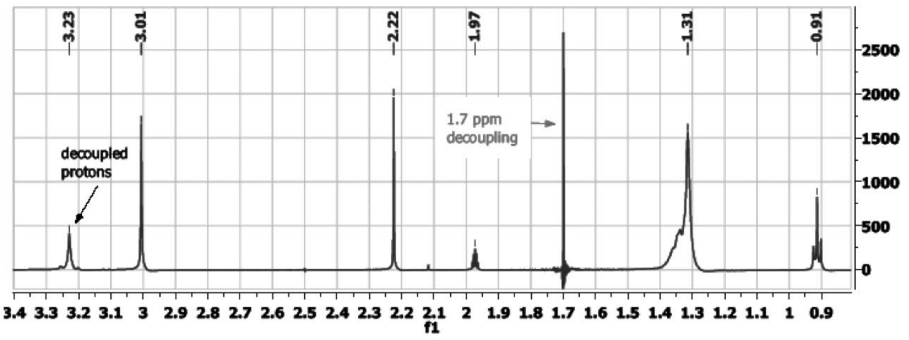
3.23
3.01
2.22
1.97
1.31
0.91
decoupled protons
1.7 ppm decoupling
f1

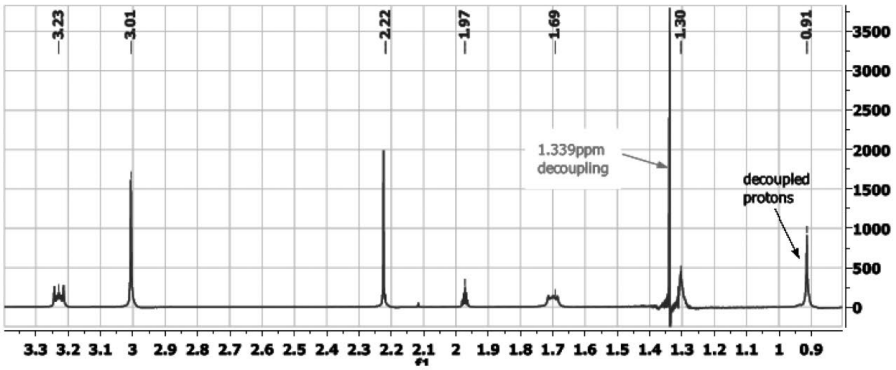
3.23
3.01
2.22
1.97
1.69
1.30
0.91
1.339ppm decoupling
decoupled protons

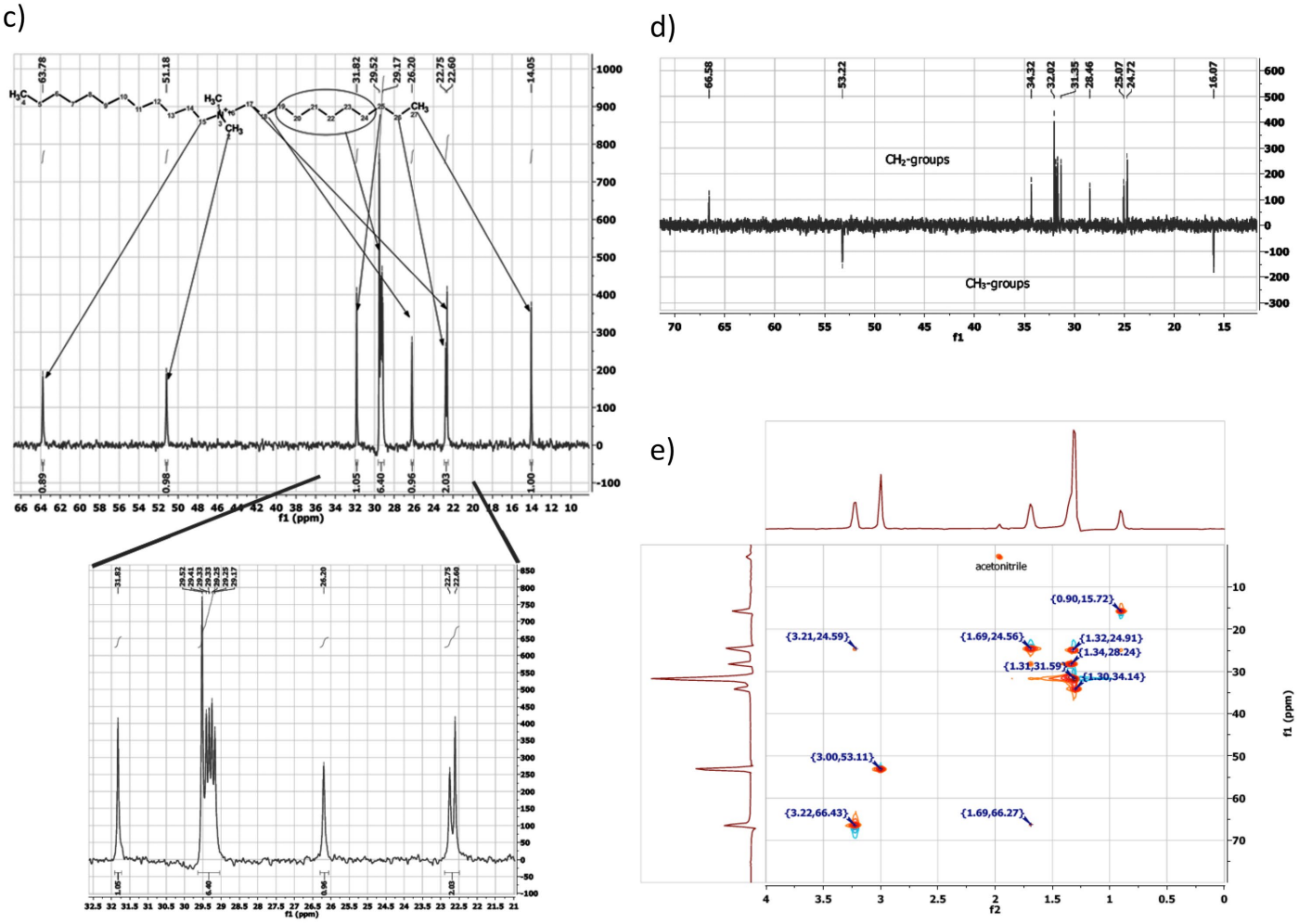

FIGURE S7: ^{1}H-NMR (a), decoupled ^{1}H-NMR (b) in acetonitrile and ^{13}C-NMR (c), ^{13}C 135DEPT and HSQC-NMR spectra in chloroform of the recrystallized dried sample of DDAB, with assignment of the peaks to the expected chemical groups. The ^{1}H-NMR spectrum measured in dry acetonitrile (MeCN) (filled in a glove box) shows the water content to be below 1 water molecule in 4 DDAB molecules. While water would be readily absorbed by the DDAB powder upon contact with the atmosphere, the water content for samples dried in the oven for a prolonged time, estimated from integrating the water peak at δ = 2.18 ppm, was less the 1 H_2O molecule in 4 DDAB molecules. This is within the measurement error associated with the minimal water content present in dry MeCN, or contamination during the measurement, thus it should be taken as an upper value. The two ethylene groups neighboring the nitrogen in the DDAB molecule form a high order spin system, as evident from the decoupled ^{1}H-NMR experiments. ^{13}C-NMR could confirm the length of the hydrocarbon chain, confirming the main component of the sample to be DDAB. 12 peaks (one of double height) could be resolved, corresponding to 13 different carbon atoms. The atoms in the middle of the chain have very similar chemical environments, and therefore appear very close to each other in the spectra. The HSQC-NMR spectrum confirms the high spin coupling between the two ethylene groups in the hydrocarbon chains next to the nitrogen.

Thermal degradation of DDAB:

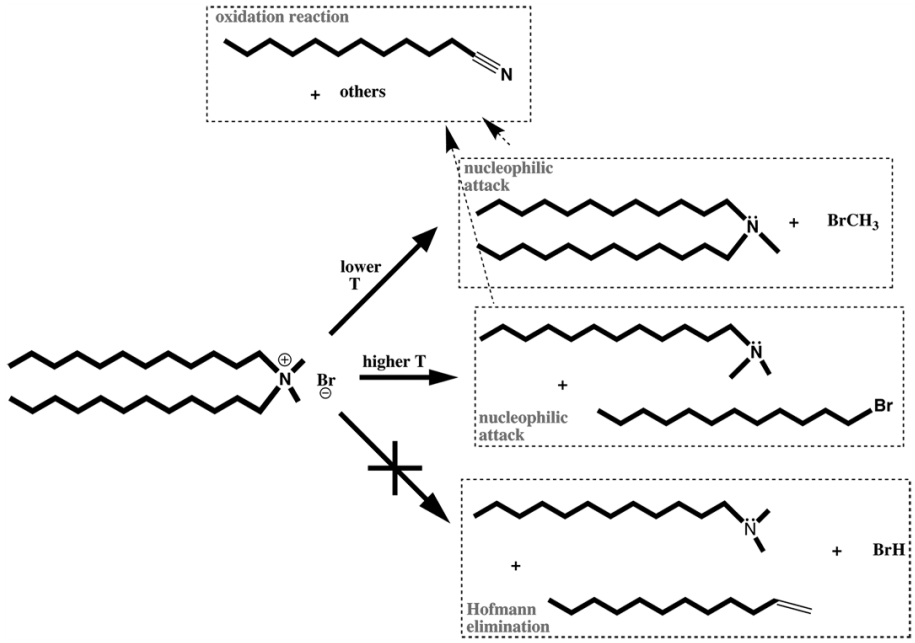

FIGURE S8: Suggested degradation pathways of DDAB above its degradation temperature of about 90°C. The degradation is most likely related to the degradation of the quaternary ammonium ion into the thermally stable amine, and subsequent N-oxidation of the amine. No oxidation is expected for the quaternary ammonium salt, itself, while the oxidation of bromide ions can be expected to activate a further decomposition of the product. To confirm the degradation pathway of DDAB, expected to be caused by nucleophilic attack by the bromide ion [Laughlin 1994], TLC analysis of samples subjected to different temperatures and exposure times was performed. Pure samples show only one spot on the TLC-plate after elution, while degraded samples exhibit additional spots. At temperatures close to the degradation temperature, the bromide attacks the nitrogen of DDA+, and displaces one of its attached methyl groups resulting in the formation of an amine (see Fig. 2), which is expected to show as the strongest spot on the TLC plate under staining with PMA. At higher temperatures, nucleophilic attack of the bromide ion on DDA+ would also have sufficient energy to detach an alkyl chain. Furthermore, trace amounts of water are expected to lead to the formation of alkanols. One should note that the decomposition via Hofmann elimination, which is often mentioned in context with quaternary ammonium salts leading to the formation of an alkene, is unlikely due to its need for a strong base (which is not the case for bromide) [Laughlin 2009]. ^{1}H-NMR of the degraded sample, whilst complex, could confirm the existence of the suggested degradation products.

Characterisation of the phase transition

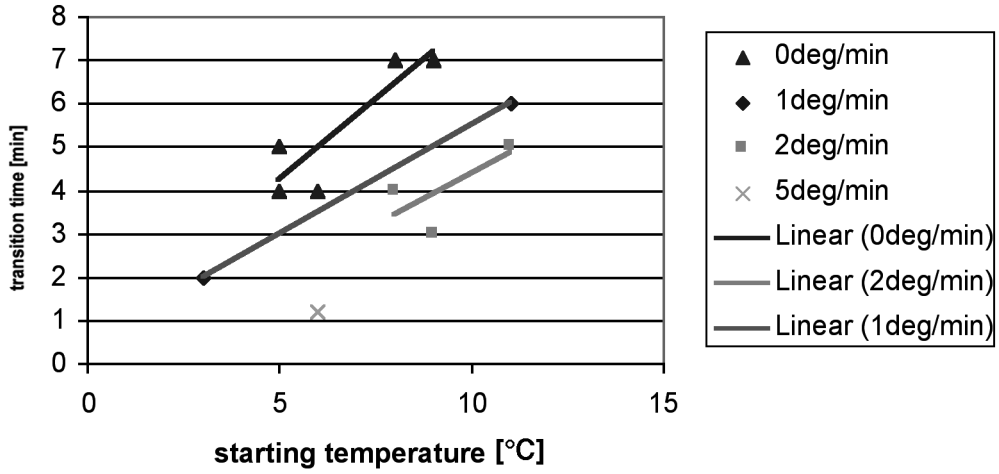

FIGURE S9: Duration Duration of the $L_\alpha \rightarrow XW_n + W$ freezing transition depending on starting temperature of the transition and on cooling rate. The lines show a least square fit to the data;

Raman spectra

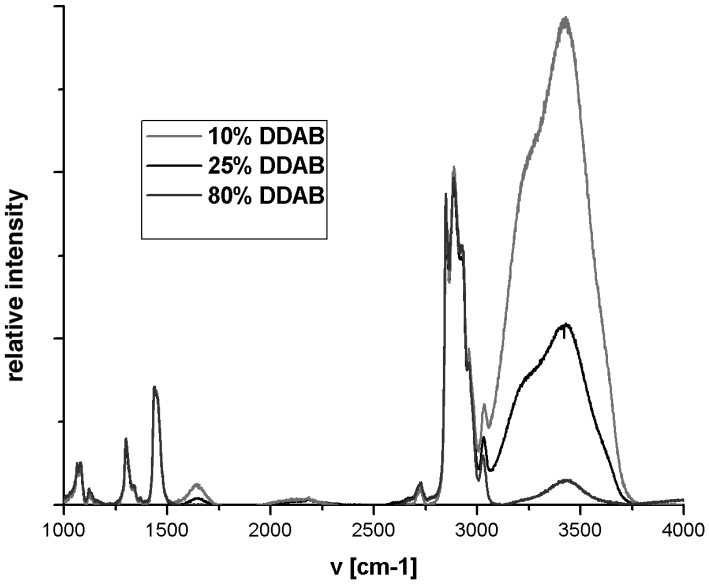

FIGURE S10: Raman spectra of aqueous DDAB solution being in the lamellar phase depending on DDAB concentration.

Sample	N [cm^{-1}] ± 10 cm^{-1}	Relative intensity[1] ± 2%
10wt% (20°C) - L_α	3220	0.66
	3440	1
	3620	0.07
10wt% (1°C) – supercooled L_α	3240	0.76
	3420	1
	3620	0.05
25wt% (20°C) - L_α	3220	0.62
	3440	1
	3620	0.05
85wt% (20°C) - L_α'	3240	0.18
	3430	1
Pure water (16°C)	3210	0.96
	3420	1
	3620	0.06
Pure water (6°C)	3210	0.92
	3420	1
	3620	0.06

TABLE S1: Raman bands corresponding to the symmetric and asymmetric stretching modes as well as an unassigned band of water in aqueous DDAB solution in the L_α or L_α' phase depending on temperature and concentration. The temperature dependence of pure water is given as a reference

[1] Setting the assymetric stretch of H_2O to 1.

Characterisation of the crystal structure in DDAB hydrated and zero-hydrate crystals

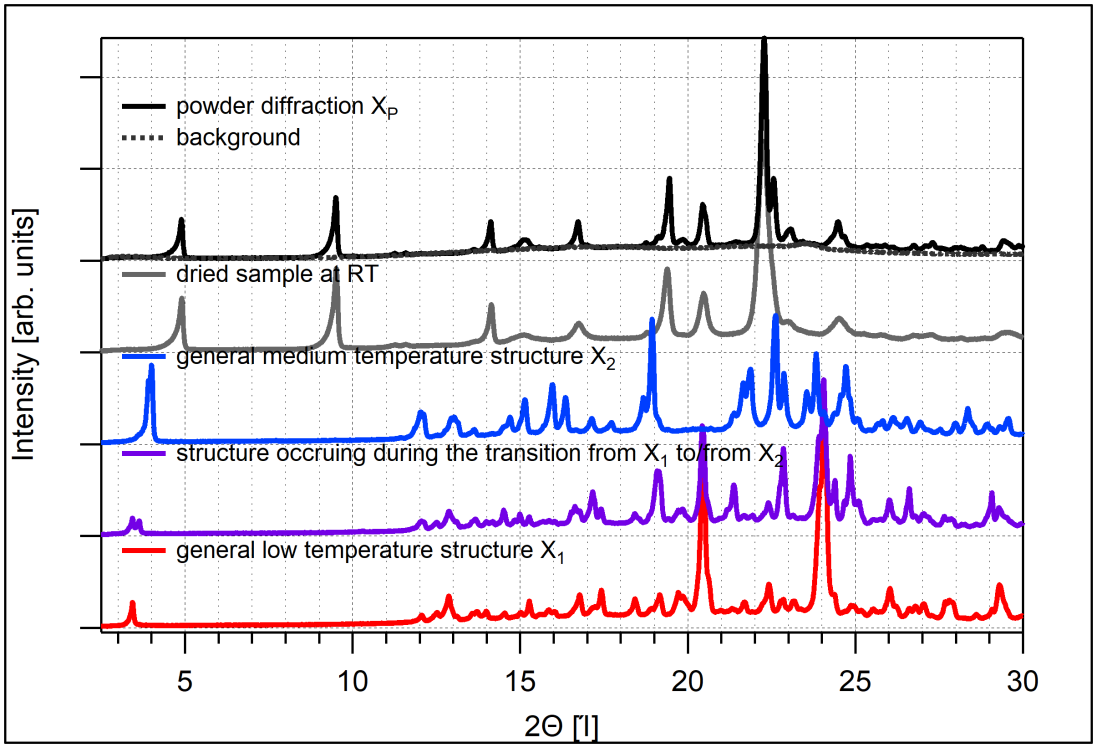

FIGURE S11: Preliminary X-ray diffraction (ISO-DebyeFlex3003) data the DDAB powder at room temperature (black line) which can also be obtained by drying a lamellar phase at room temperature. The X-ray diffraction data of the 'white' phase recorded below 14°C (red line) (tested for samples between 10-90 wt%) has a distinct character. Upon heating another diffraction pattern can occur (purple line), which changes into the comparably stable (blue) line, upon further heating (approx. 18°C) or drying.